







 Cite this: *New J. Chem.*, 2022, 46, 18751

Influence of bridging and chelating co-ligands on the distinct single-molecule magnetic behaviours in ZnDy complexes†

 Anangamohan Panja, *^{ab} Zvonko Jagličić, ^c Radovan Herchel, ^d
Paula Brandão ^e and Narayan Ch. Jana ^a

Four new heterometallic ZnDy complexes, [ZnDy(L)(NO₃)₃(py)]·CH₂Cl₂ (**1**) (py stands for pyridine), [ZnDy(L)(μ-OAc)(OAc)₂]·3H₂O (**2**), [ZnDy(L)(μ-OAc)(OAc)(NO₃)] (**3**), and [ZnDy(L)(μ-piv)(piv)₂][ZnDy(L)(μ-piv)(piv)(OAc)]·1.5H₂O (**4**), have been synthesized from a methyl substituted *o*-vanillin based compartmental Schiff base ligand, *N,N'*-bis(3-methoxy-5-methylsalicylidene)-1,2-phenylenediamine (H₂L), in association with various secondary co-ligands like acetate (OAc), nitrate and pivalate (piv), and magneto-structurally characterised. They possess a nearly identical [Zn(II)–Dy(III)] core, bridged by the phenoxo-O atoms of the compartmental Schiff base ligand. Magnetic studies revealed the distinct single-molecule magnetic (SMM) behaviours through single to multiple relaxation channels, in which **1**, **2** and **4** can display slow relaxation of magnetisation at a zero dc field, the performance of which can be further improved by applying a magnetic field at the expense of the reduction of under barrier relaxation processes, while **3** shows only field-induced weaker slow magnetic relaxation behaviours. *Ab initio* calculations were performed for the in-depth understanding of the magnetic dynamics in these complexes. The difference in the magnetic behaviours of the four complexes can be ascribed to the effect of bridging/chelating co-ligands in these complexes. Therefore, the present report highlights that the magnetic anisotropy is sensitive to the bridging/chelating co-ligands used, leading to the distinct magnetic dynamics in these systems.

 Received 31st July 2022,
Accepted 5th September 2022

DOI: 10.1039/d2nj03793a

rsc.li/njc

Introduction

The literature has witnessed the rapid development of single-molecule magnets (SMMs), characterised by the slow relaxation of magnetisation, during the last few decades because of their rich classical and quantum properties that are suitable for their potential applications as components of high-density information storage, molecular spintronics and quantum computing devices.¹ The 4f elements, particularly Dy(III) ions, were

widely utilised for the construction of SMM materials due to their large angular momentum *J* arising from the intrinsic strong spin–orbit coupling, leading to high effective energy barriers for magnetisation reversal (*U*_{eff}).^{2,3} The rapid development of Dy-based SMMs shows the continuous improvement of the SMM character in terms of the magnetisation reversal barrier and the blocking temperature (*T*_B).^{4,5} Despite these apparent successes, it still remains a challenge to understand the complicated magnetic behaviours of Dy-based molecular magnets, which can be influenced by several factors *viz.* spin–orbit coupling, symmetry imposed single-ion magnetic anisotropy, magnetic interactions, and crystal-field effects.⁶ Moreover, the quantum tunnelling of magnetisation (QTM) is hard to avoid as it is influenced by several factors like dipole–dipole interactions and transverse anisotropy, which led to the greatly reduced SMM performance.

Usually, a high axial symmetry like *D*_{6h}, *D*_{5h}, *D*_{4h}, *D*_{4d} and *C*_{∞v} around the Dy(III) ions coupled with an axial crystal field favours the suppression of QTM and increases the magnetic anisotropy, rendering the prominent thermally active Orbach relaxation and hence enhancing the performance of Dy-based SMMs.⁷ Another strategy utilises the introduction of magnetic

^a Department of Chemistry, Panskura Banamali College, Panskura RS, WB, 721152, India. E-mail: ampanja@yahoo.co.in

^b Department of Chemistry, Gokhale Memorial Girls' College, 1/1 Harish Mukherjee Road, Kolkata, 700020, India

^c Institute of Mathematics, Physics and Mechanics & Faculty of Civil and Geodetic Engineering, University of Ljubljana, Jadranska 19, 1000, Ljubljana, Slovenia

^d Department of Inorganic Chemistry, Faculty of Science, Palacký University, 17. listopadu 12, 77146, Olomouc, Czech Republic

^e Department of Chemistry, CICECO-Aveiro Institute of Materials, University of Aveiro, 3810-193, Aveiro, Portugal

† Electronic supplementary information (ESI) available: Fig. S1–S20 and Tables S1–S14. CCDC 2181879–2181882 for complexes 1–4. For ESI and crystallographic data in CIF or other electronic format see DOI: <https://doi.org/10.1039/d2nj03793a>

coupling between the Dy(III) ions, which plays an important role in enhancing the magnetic anisotropy and the reduction of QTM.⁸ Therefore, binuclear Dy-based SMMs could be better candidates for tuning both intramolecular magnetic coupling and individual magnetic anisotropy to achieve high performance SMMs. In addition to the 4f–4f interaction, the 3d–4f interaction is also quite useful for the reduction of QTM, leading to high performance of 3d–4f SMMs.⁹ Moreover, the recent studies on 3d–4f complexes with diamagnetic 3d metal ions such as Zn(II) or Co(III) disclosed the significant enhancement of the magnetisation reversal barrier in comparison to their mononuclear lanthanide analogues.¹⁰ It is suggested that the introduction of a diamagnetic 3d ion in the close vicinity of the Dy(III) centre, connected through O bridge(s), induces a large charge polarisation on the bridging oxygen atom, which favours uniaxial magnetic anisotropy and hence increases the magnetisation reversal barrier.¹¹ Additionally, the inclusion of diamagnetic 3d metal ions may indeed induce an internal dilution effect of the Dy(III) ion that reduces the dipolar interactions and hence QTM.¹²

Classical salen-type compartmental Schiff base ligands derived from *o*-vanillin were widely used for the construction of heteronuclear 3d–4f complexes, because they provide two distinct coordination compartments to selectively accommodate 3d metal ions through a smaller and inner compartment with N₂O₂ donor sites and lanthanide ions through a larger and outer compartment with O-donor atom rich coordination sites.¹³ The initial aim of introducing 3d–4f magnetic coupling was to enhance the performance of SMMs involving paramagnetic Ni–Ln, Cu–Ln and Co–Ln complexes.¹⁴ Among these heteronuclear 3d–4f SMMs, however, diamagnetic 3d elements containing species like Zn–Ln complexes exhibited pronounced SMM performance than the most paramagnetic 3d–4f analogues and the homodinuclear Dy-based SMMs.^{10,11} We are now working with Schiff base ligands derived from a methyl derivative of *o*-vanillin at the *para* position with respect to the phenolic-OH group to explore coordination chemistry, and the resulting Dy or Zn–Dy complexes displayed slow relaxation of magnetisation.¹⁵ More recently, a Schiff base ligand, *N,N'*-bis(3-methoxy-5-methylsalicylidene)-1,2-phenylenediamine, (H₂L), derived from 2-hydroxy-3-methoxy-5-methylbenzaldehyde (Me-val) and *o*-phenylenediamine (Scheme 1), has been used to construct angular Zn₂Dy complexes.¹⁶ Although all these complexes displayed slow relaxation of magnetisation, the non-ideal arrangement of phenolate donors are mainly responsible for the weaker SMM character in these complexes. It was observed that π – π stacking interactions involving aromatic rings of the Schiff base ligands, especially the involvement of the aromatic ring of the *o*-phenylenediamine component of the Schiff base ligand, enforces the angular arrangement of the Zn–Dy–Zn centres in these complexes, leading to a weaker SMM performance, and further suggests that the linear Zn–Dy–Zn arrangement or simple Zn–Dy complexes could bring the ideal arrangement of phenolate donor atoms around Dy(III) centres to enhance the magnetic anisotropy and SMM character in these systems.¹⁶ With this view, we continue to use this compartmental Schiff base H₂L as a primary ligand in combination with various secondary co-ligands

such as acetate (OAc), nitrate and pivalate (piv) to construct superior Zn–Dy SMMs. Accordingly, in the present endeavour, we report the magneto-structural studies of four new ZnDy complexes, [ZnDy(L)(NO₃)₃(py)]·CH₂Cl₂ (1), [ZnDy(L)(μ -OAc)(OAc)₂]·3H₂O (2), [ZnDy(L)(μ -OAc)(OAc)(NO₃)] (3), and [ZnDy(L)(μ -piv)(piv)₂][ZnDy(L)(μ -piv)(piv)(OAc)]·1.5H₂O (4), where py stands for pyridine. The magnetic studies revealed that all these complexes display the distinct slow relaxation of magnetisation, well-tuned by the bridging and chelating ligands. The magnetic data were analysed and theoretical calculations were further performed to interpret the experimental results in these complexes.

Experimental section

Materials and physical measurements

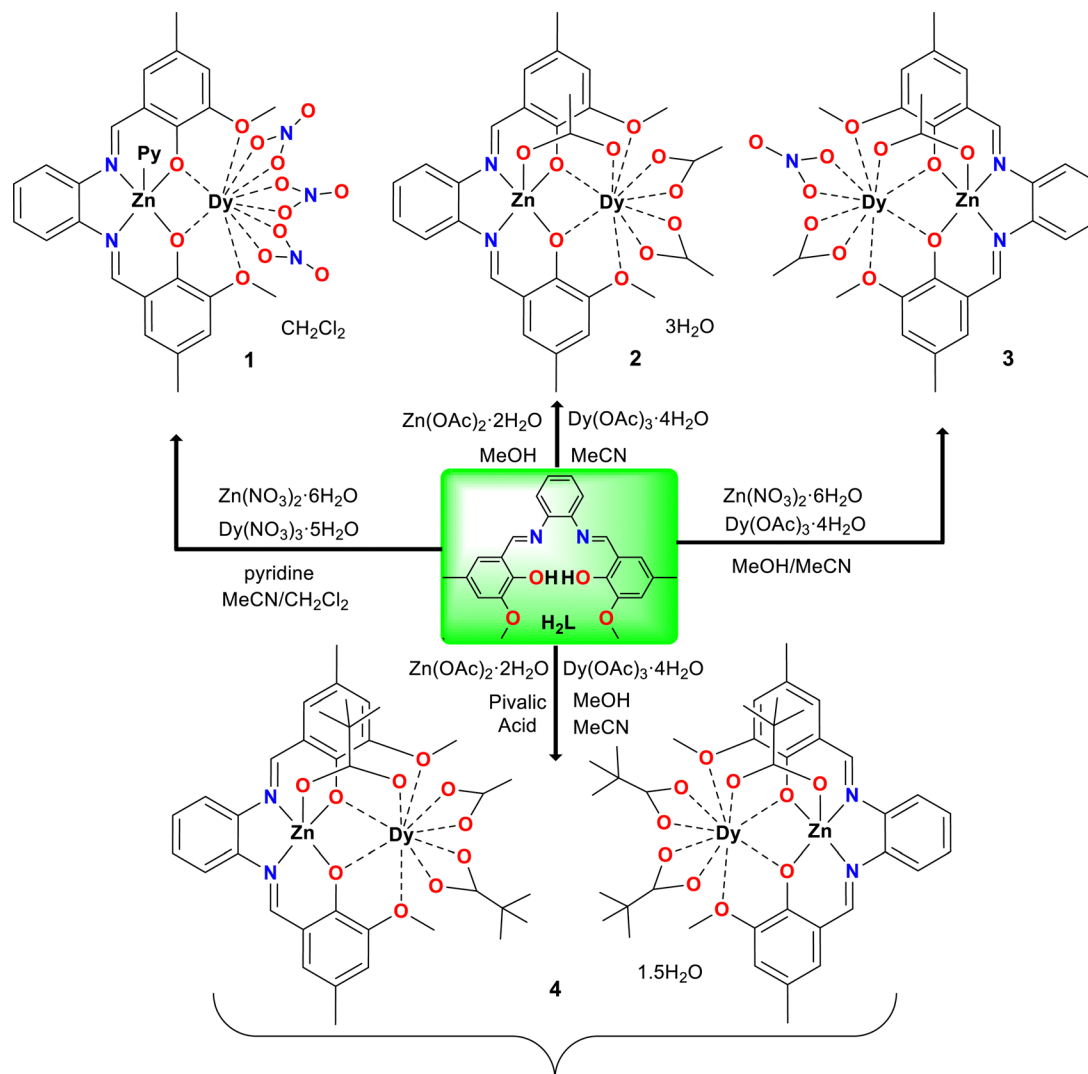
All reagent grade chemicals and solvents were obtained commercially and used without further purification. 2-Hydroxy-3-methoxy-5-methylbenzaldehyde (Me-val) and *N,N'*-bis(3-methoxy-5-methylsalicylidene)-1,2-phenylenediamine (H₂L) were synthesized according to the literature reported methods.¹⁶ All manipulations were carried out under aerobic conditions. Elemental analyses (carbon, hydrogen and nitrogen) were conducted using a PerkinElmer 240C elemental analyser. The FTIR spectra of the complexes were recorded using a Thermo Scientific Nicolet iS5 FTIR spectrometer using a universal ATR sampling accessory in the range of 4000 to 400 cm⁻¹. Direct current (dc) magnetic susceptibility measurements were carried out using a Quantum Design MPMS-XL-5 magnetometer under a constant magnetic field of 1000 Oe in the temperature range of 2 to 300 K. Alternating current (ac) susceptibility measurements under both the zero static field and applied dc fields were performed applying an oscillating ac field of 1 or 6 Oe with ac frequencies ranging from 0.1 (or 1) to 1400 Hz. The diamagnetic contribution of the samples and the sample holders were subtracted as usual from the collected data.

Synthesis of [ZnDy(L)(NO₃)₃(py)]·CH₂Cl₂ (1)

A mixture of Zn(NO₃)₂·6H₂O (60 mg, 0.2 mmol), H₂L (80 mg, 0.2 mmol) and pyridine (50 mg, 0.6 mmol) in 30 mL of MeCN/CH₂Cl₂ (1 : 2, v/v) was stirred for 15 min. Then, Dy(NO₃)₃·5H₂O (88 mg, 0.2 mmol) was added to the mixture and stirring was continued for another 2 h. The resulting yellow solution was then filtered and the filtrate was left undisturbed at ambient temperature for slow evaporation. Yellow needle crystals suitable for X-ray diffraction were obtained after a week. Yield: 125 mg (64%) based on Dy(NO₃)₃·5H₂O. Anal. calcd for C₃₀H₂₇N₆O₁₃Cl₂ZnDy: C 36.83%, H 2.78%, N 8.59%. Found: C 36.89%, H 3.12%, N 8.42%.

Synthesis of [ZnDy(L)(μ -OAc)(OAc)₂]·3H₂O (2)

Zn(OAc)₂·2H₂O (44 mg, 0.2 mmol) was added to a solution of Schiff base H₂L (80 mg, 0.2 mmol) in 30 mL of MeOH/MeCN (1 : 1, v/v), and the mixture was stirred for about 15 min. Dy(OAc)₃·4H₂O (82 mg, 0.2 mmol) was then added to the mixture. After being stirred for about 2 h, the resulting yellow solution was filtered and the filtrate was left undisturbed at



Scheme 1 Synthetic route to complexes 1–4.

ambient temperature for slow evaporation. Yellow needle crystals suitable for X-ray diffraction were obtained after one week. Yield: 98 mg (57%) based on $\text{Dy}(\text{OAc})_3 \cdot 4\text{H}_2\text{O}$. Anal. calcd for $\text{C}_{30}\text{H}_{37}\text{N}_2\text{O}_{13}\text{ZnDy}$: C 41.83%, H 4.33%, N 3.25%. Found: C 41.59%, H 4.42%, N 3.12%.

Synthesis of $[\text{ZnDy}(\text{L})(\mu\text{-OAc})(\text{OAc})(\text{NO}_3)]$ (3)

Complex 3 was prepared adopting a method very similar to the synthesis of 2 except that $\text{Zn}(\text{OAc})_2 \cdot 2\text{H}_2\text{O}$ was replaced by $\text{Zn}(\text{NO}_3)_2 \cdot 6\text{H}_2\text{O}$. Colour: yellow. Yield: 97 mg (62%) based on $\text{Dy}(\text{OAc})_3 \cdot 4\text{H}_2\text{O}$. Anal. calcd for $\text{C}_{28}\text{H}_{28}\text{N}_3\text{O}_{11}\text{ZnDy}$: C 41.50%, H 3.48%, N 5.19%. Found: C 41.69%, H 3.52%, N 5.10%.

Synthesis of $[\text{ZnDy}(\text{L})(\mu\text{-piv})(\text{piv})_2][\text{ZnDy}(\text{L})(\mu\text{-piv})(\text{piv})(\text{OAc})] \cdot 1.5\text{H}_2\text{O}$ (4)

$\text{Zn}(\text{OAc})_2 \cdot 2\text{H}_2\text{O}$ (44 mg, 0.2 mmol) and H_2L (80 mg, 0.2 mmol) were added in 30 mL of MeOH/MeCN (1 : 1, v/v) with stirring for 15 min. Thereafter, pivalic acid (63 mg, 0.6 mmol), $\text{Dy}(\text{OAc})_3 \cdot 4\text{H}_2\text{O}$ (82 mg, 0.2 mmol) and Et_3N (150 μL , 1.0 mmol) were

added with continuous stirring and it was stirred for another 2 h. Then the resulting yellow solution was filtered and the filtrate was left undisturbed at ambient temperature for slow evaporation. Yellow needle crystals of the X-ray diffraction quality were obtained after a week. Yield: 111 mg (54%) based on $\text{Dy}(\text{OAc})_3 \cdot 4\text{H}_2\text{O}$. Anal. calcd for $\text{C}_{75}\text{H}_{95}\text{N}_4\text{O}_{21.50}\text{Zn}_2\text{Dy}_2$: C 48.63%, H 5.17%, N 3.03%. Found: C 48.39%, H 5.22%, N 3.31%.

Single crystal X-ray diffraction analysis

The single-crystal diffraction data of 1–4 were collected at 150 K using Bruker Kappa Apex-II CCD and Bruker D8 QUEST diffractometers equipped with a Photon 100 area detector operating with a graphite monochromated Mo-K α radiation ($\lambda = 0.71073 \text{ \AA}$). The diffraction data were collected by scanning over φ and ω directions and were averaged during refinement cycles. The unit cell determination, data integration and reduction were carried out using the Bruker SAINT plus software. The reflection data were then corrected for absorption by the multi-scan method

implemented in the SADABS program.¹⁷ The crystal structures of **1–4** were solved by the direct methods and refined by means of the full matrix least-square technique based on F^2 using the SHELX-2018 program.¹⁸ All non-hydrogen atoms were refined with anisotropic thermal parameters. Hydrogen atoms connected to carbon atoms were placed in geometrically idealised positions and refined in a riding model with fixed thermal parameters of 1.2 or 1.5 times of the corresponding parent atoms, while hydrogen atoms attached to some oxygen atoms of lattice water molecules were located on the difference Fourier map and refined with O–H constrained distances. The other details of crystal data and structure refinement parameters are presented in Table S1 (ESI[†]). The crystal structures were developed using the program MERCURY-4.3.1 and the POV-ray software.

Theoretical calculations

The ORCA 5.0 software was employed for DFT and *ab initio* calculations.¹⁹ The Douglas–Kroll–Hess (DKH) Hamiltonian was utilized to treat relativistic effects²⁰ together with the Gaussian finite nucleus model.²¹ The relativistic basis sets were applied as follows: SARC2-DKH-QZVP for Dy, DKH-def2-TZVP for Zn, N, and O and DKH-def2-SVP for C and H atoms.²² The auxiliary basis set SARC/J²³ and the AutoAux generation procedure²⁴ together with the chain-of-spheres (RIJCOSX) approximation to the exact exchange²⁵ were used to speed up the calculations. The molecular fragments of the complexes were extracted from experimental X-ray structures and only hydrogen atom positions were optimized with the help of the PBE0 hybrid DFT functional²⁶ and density dependent atom-pairwise dispersion correction (D4).²⁷ The calculated data were visualized using the VESTA 3 program.²⁸

Results and discussion

The salen-type *o*-vanillin based compartmental Schiff base ligand has been widely used for the construction of heterometallic 3d–4f complexes with interesting magnetic properties.^{13,29–43} We are now working with a methyl substituted *o*-vanillin derivative for the development of coordination chemistry with anticipation that the methyl substitution at the *para* position with respect to the phenolic-OH group would increase the electron density on the phenolate oxygen, and thus may have a significant influence on the electronic structure and the crystal field around the Dy(III) ion.^{15,16} In continuation to our recent effort, the Schiff base ligand H₂L was allowed to react with Zn(NO₃)₂·6H₂O and Dy(NO₃)₃·5H₂O in a 1:1:1 molar ratio in the presence of excess pyridine in a mixed solvent of MeCN/CH₂Cl₂ (1:2, v/v) to produce [ZnDy(L)(NO₃)₃(py)]·CH₂Cl₂ (**1**) in reasonable yields. Similarly, complexes [ZnDy(L)(μ-OAc)(OAc)₂]·3H₂O (**2**), [ZnDy(L)(μ-OAc)(OAc)(NO₃)] (**3**), and [ZnDy(L)(μ-piv)(piv)₂][ZnDy(L)(μ-piv)(piv)(OAc)]·1.5H₂O (**4**) were synthesized from the Schiff base ligand H₂L using different co-ligands to tune the coordination geometry and the coordination environment around the metal centres. All these complexes were routinely characterized by elemental analyses and the IR spectroscopically (Fig. S1, ESI[†]), and the bulk crystalline phase

purity of the complexes was checked by the powder X-ray diffraction (PXRD) study (Fig. S2, ESI[†]).

Description of the crystal structures of 1–4

The crystal structures of complexes **1–4** are depicted in Fig. 1–3, and the selected bond distances are listed in Table 1. All the complexes crystallized in the monoclinic unit cell but in different space groups of $P2_1/n$ in **1**, $C2/c$ in **2** and $P2_1/c$ in **3** and **4** (Table S1, ESI[†]). In all these complexes, the connectivity of the doubly deprotonated Schiff base ligand L is very similar in that the inner N₂O₂ core of the ligand accommodates Zn(II) ions, while the outer O₂O'₂ core includes Dy(III) ions. Additionally, in **1** (Fig. 1), the Zn(II) ion is apically coordinated with the pyridyl group and the Dy(III) ion is chelated by three bidentate nitrate ions, resulting in ZnN₃O₂ and DyO₁₀ coordination environments around Zn(II) and Dy(III) ions, respectively. In **2** and **3** (Fig. 2), an acetate ion bridges the metal centres in a μ-1,3 (*syn syn*) bridging fashion and two acetate ions in **2** and one acetate group and one nitrate ion in **3** coordinate the Dy(III) ions as bidentate chelating ligands, resulting in ZnN₂O₃ and DyO₉ coordination environments around Zn(II) and Dy(III) ions, respectively, in both the complexes. Although the structure of **4** (Fig. 3) is very similar to that found in **2**, the asymmetric unit consists of two different complex molecules with formulas [ZnDy(L)(μ-piv)(piv)₂] and [ZnDy(L)(μ-piv)(piv)(OAc)] and the crystal voids accommodate different numbers of water of crystallisation molecules in these complexes. The Zn(II) ions are invariably five-coordinated with square-pyramidal geometry in all these complexes, in which the metal centre is placed slightly away from the mean square N₂O₂ plane from the inner core of the Schiff base ligand (0.288–0.616 Å, range) toward the axially coordinated atoms, typical for Zn(II) complexes.^{29–43} The Zn–O and Zn–N bond distances vary in the range of 1.964(6)–2.055(8) Å in **1–4**.^{29–43}

The geometry of a ten-coordinate Dy(III) ion in **1** was analysed by the continuous-shape measure (CShMs) method implemented

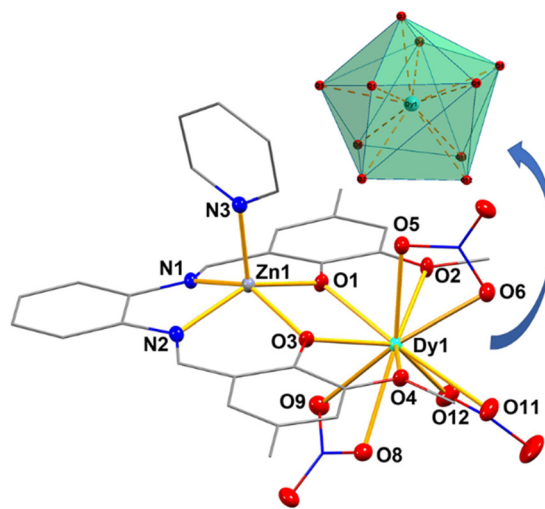


Fig. 1 Crystal structure of complex **1** with ellipsoid (30% probability) plots of the metal coordination sphere only and the local coordination geometry around the Dy(III) centre.

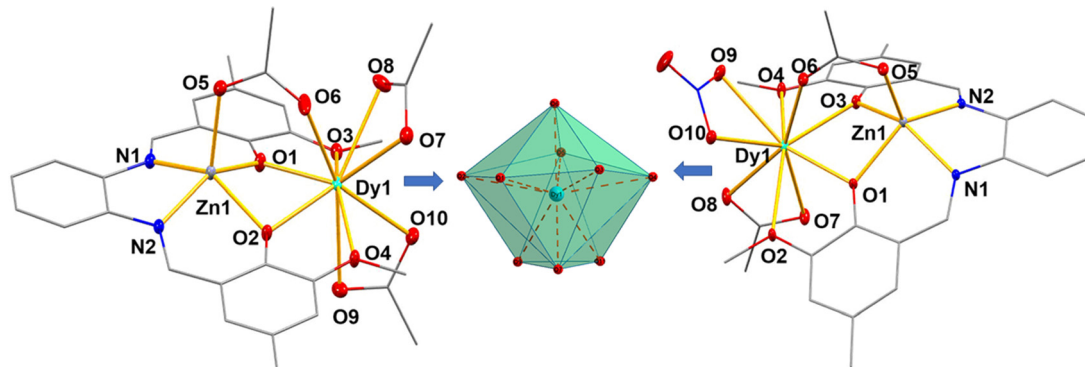


Fig. 2 Crystal structures of complexes **2** (left) and **3** (right) showing ellipsoid (30% probability) plots of the metal coordination sphere only and the local coordination geometry around the Dy(III) centres in **2** and **3** (middle).

in the Shape 2.1 software using the crystallographic coordinates that reveals Sphenocorona geometry with C_{2v} symmetry as suggested by a minimum CShM value of 3.022 (Table S2, ESI[†]).⁴⁴ Similar calculations disclose that the Dy(III) centres adopt a nine-coordinate muffin like geometry with C_s symmetry in **2** (CShM = 2.947) and **3** (CShM = 2.990), while the Dy(III) centres in two crystallographically distinguishable complex molecules in **4** have nine-coordinate muffin like geometry with C_s symmetry (DyB, CShM = 3.263) and spherical capped square antiprism with D_{4d} symmetry (DyA, CShM = 2.640) (Table S3, ESI[†]). The Dy–O bond distances with phenolate-O atoms are expected to be shorter and vary in the range of 2.290(2)–2.378(8) Å, while the Dy–O bond distances of the methoxy group are significantly longer and span in the range of 2.553(2)–2.678(1) Å.^{29–43} The Dy–O bond distances of acetate groups in **2**, **3** and **4** and nitrate ions in **1** and **3** are in the intermediate range and vary in between 2.342(2)–2.4456(11) Å and 2.439(2)–2.519(2) Å, respectively. A mixed impression has been observed for the Dy–O bond distances of pivalate groups in **4** as the Dy–O bond distances with bridging pivalate groups (2.316(8) and 2.332(7) Å) are significantly shorter and are comparable to the Dy–O bond distances with phenolate-O atoms, while it falls again in the intermediate range (2.377(8)–2.428(6) Å) for the chelating bidentate pivalate ligands. Inspection of the crystal packing

reveals that the neighbouring molecules in these complexes interact with each other through different kinds of weak non-covalent interactions. The common feature is that the ligands from the adjacent complex molecules are involved in the $\pi \cdots \pi$ interaction in all the systems (Fig. S3–S6, ESI[†]). Additionally, one of the coordinated nitrate ions establishes nonconventional C–H \cdots O hydrogen bonding in **1**. In **2** and **4**, some of the coordinated acetate/pivalate ions engage in the hydrogen bonding interaction with lattice water molecules. The closest intermolecular Dy \cdots Dy separations are found to be 8.650, 8.125, 7.122 and 8.835 Å for **1–4**, respectively.

Magnetic study

The direct-current (dc) magnetic susceptibility data of polycrystalline samples of **1–4** were collected in a temperature range of 2–300 K under a constant applied dc field of 1000 Oe and plotted as a function of $\chi_{\text{mol}}T$ vs. T (Fig. 4). The room temperature $\chi_{\text{mol}}T$ products of **1–4** are 14.0, 13.6, 15.1 and 14.3 emu K mol⁻¹, respectively, which are close to the theoretical $\chi_{\text{mol}}T$ value of

Table 1 Bond distances around metal coordination spheres in **1–4**

Bond	Distances				
	1	2	3	4 A B	
Dy–O1	2.3163(18)	2.3033(10)	2.3014(15)	2.317(7)	2.369(7)
Dy–O2	2.6395(19)	2.6788(11)	2.5532(15)	2.665(8)	2.658(9)
Dy–O3	2.2906(18)	2.3377(10)	2.3082(15)	2.378(8)	2.330(7)
Dy–O4	2.5743(19)	2.5624(11)	2.5904(16)	2.574(9)	2.554(9)
Dy–O5	2.475(2)	—	—	—	—
Dy–O6	2.452(2)	2.3670(12)	2.3524(17)	2.316(8)	2.332(7)
Dy–O7	—	2.4456(11)	2.3782(18)	2.397(7)	2.428(6)
Dy–O8	2.478(2)	2.4157(12)	2.3424(18)	2.377(8)	2.405(7)
Dy–O9	2.519(2)	2.4145(11)	2.4399(17)	2.390(8)	2.412(7)
Dy–O10	—	2.3919(11)	2.4643(16)	2.412(9)	2.420(7)
Dy–O11	2.488(2)	—	—	—	—
Dy–O12	2.450(2)	—	—	—	—
Zn–O1	1.9788(18)	2.0064(10)	2.0029(14)	1.989(7)	1.994(8)
Zn–O3	2.0013(18)	1.9957(10)	2.0123(15)	2.017(6)	2.034(7)
Zn–O5	—	2.0024(11)	1.9658(16)	1.989(6)	1.964(6)
Zn–N1	2.024(2)	2.0301(12)	2.0343(17)	2.026(8)	2.055(8)
Zn–N2	2.055(2)	2.0341(12)	2.0538(17)	2.043(8)	2.027(9)
Zn–N3	2.042(2)	—	—	—	—
Dy \cdots Zn	3.470 (1)	3.339(1)	3.345(1)	3.344(1)	3.513(8)

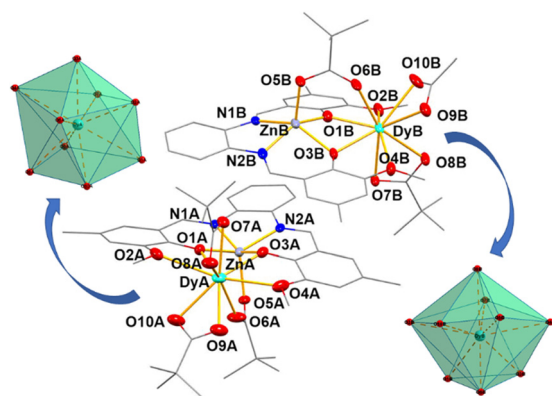


Fig. 3 Crystal structures of both complex molecules in **4** displaying ellipsoid (30% probability) plots of the metal coordination sphere only and the local coordination geometry around the Dy(III) centres.

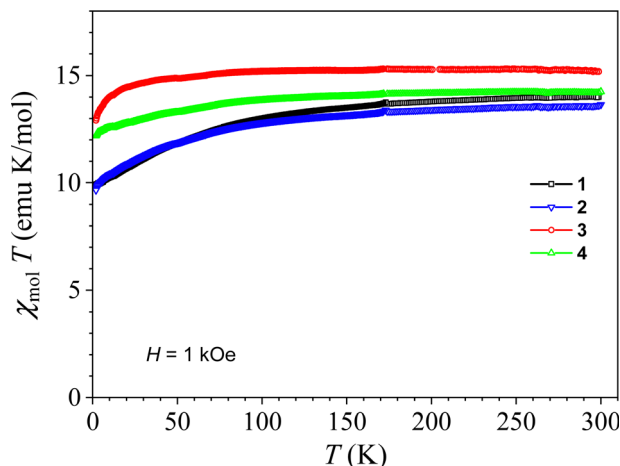


Fig. 4 Temperature dependence of the product $\chi_{\text{mol}}T$ at a 1000 Oe magnetic field for **1–4**. The magnetic data are scaled per one Dy(III) ion.

14.17 emu K mol⁻¹ as estimated for an isolated Dy(III) ion (⁶H_{15/2}, $g = 4/3$). As the temperature is lowered, the $\chi_{\text{mol}}T$ products decrease gradually from 300 K to 100 K, below which the $\chi_{\text{mol}}T$ products decrease more rapidly. The overall magnetic behaviour is attributed to the progressive thermal depopulation of Stark sublevels arising from the splitting of the ground multiplet of the Dy(III) ion and/or the possible intermolecular antiferromagnetic dipole–dipole interaction among Dy(III) ions manifested particularly at low temperatures.⁴⁵ The isothermal magnetization (M) data at 2 K as a function of the dc field (H) of these complexes (Fig. S7, ESI[†]) display a relatively rapid increase at low magnetic fields, followed by a gradual linear-like increase at high fields to attain finally the maximum values of $4.9 N_A\mu_B$ for **1**, $4.9 N_A\mu_B$ for **2**, $6.0 N_A\mu_B$ for **3** and $5.2 N_A\mu_B$ for **4** at the highest applied magnetic field of 5 T. These values are far from the saturation value of a Dy(III) ion of $10 N_A\mu_B$, which is consistent with the presence of significant magnetic anisotropy and/or low-lying excited states in these Dy(III) complexes.⁴⁶

The magnetic dynamics of **1–4** was explored by means of temperature- and frequency-dependent alternating-current (ac) susceptibility measurements both at zero and applied dc fields with the aim of unveiling if they display the slow relaxation of magnetisation and, if so, to accomplish a comparative dynamic magnetic behaviour of these closely related compounds. To explore the effect of the external dc field on the relaxation process, the dc field scans were obtained for a set of frequencies spanning between 1 and 1400 Hz at 2 K (Fig. S8–S11, ESI[†]), which show the out-of-phase χ''_{mol} signals for all complexes except **3** at the zero dc field. With the increasing dc field up to 10 kOe, the out-of-phase signal varies, but differently for individual frequencies, and it is clearly visible in Fig. S8–S11 (ESI[†]) for **1–4**, respectively, that the maximal responses of the out-of-phase susceptibility component appear at around 1000 Oe dc field for **1**, **2** and **4** and at about 600 Oe dc field for **3** and thereafter the response decreases progressively with the increase in the magnetic field, indicating that these external magnetic fields could bring the slowest possible relaxation processes in respective compounds. Interestingly, when the same

data sets have been rearranged to the frequency dependence of the ac susceptibility components for a set of external magnetic fields (Fig. S8–S11, ESI[†]), a complex frequency-dependent out-of-phase ac susceptibility is observed. As can be seen from these figures, at the zero dc field, only **1**, **2** and **4** display characteristic χ''_{mol} signals, and no signal was detected for **3** in the measured frequency range from 1 to 1400 Hz. Remarkably, the χ''_{mol} vs. frequency plots show the presence of two possible relaxation channels, *i.e.*, high frequency (HF) and low frequency (LF) relaxation channels in **1**, **2** and **4**. At the low dc field, only one relaxation process is observed in the HF region, and this HF relaxation process is progressively quenched with the increasing field and disappears completely for the fields stronger than 1000 Oe. Therefore, only the relaxation process in the low frequency region can be clearly identified at higher magnetic fields and the signal strength is found to be the largest at around 1000 Oe magnetic field. However, none of the frequency regions show any maximum within the measured frequency window, but it is apparent that, at the zero dc field, the HF relaxation pathway is the most dominant one as suggested by the larger signals, and at the field 1000 Oe, the HF pathway is almost quenched and the corresponding signals in the LF region become larger, and therefore a detailed ac magnetic susceptibility studies were carried out both at zero and 1000 Oe dc fields for better understating the relaxation dynamics in these complexes. On the other hand, the χ''_{mol} signal increases with the increasing applied dc field mainly in the HF region and attains a maximum value at the 600 Oe dc field and thereafter attenuates again with the increase in the magnetic field (Fig. S10, ESI[†]), indicating that the 600 Oe magnetic field is suitable for examining the slow magnetic relaxation behaviour in complex **3**. Interestingly, when the dc field is further increased, the signals in the HF region progressively decrease with the concomitant increase of the signal tails in the LF region, and the signals in the LF region become larger when the dc field is reached to 2000 Oe, which indicates the opening of a new relaxation channel in the LF region at a 2000 Oe field, and notably, in this applied field, the signal strength throughout the frequency window is comparable. Clearly, the higher external magnetic field supports the low-frequency relaxation channel at the expense of the high-frequency mode. The appearance of a second maximum in χ''_{mol} signals at the lowest measured frequency (1 Hz) in the field sweep data at 2 K is consistent with the above fact (Fig. S11, ESI[†]). Therefore, detailed frequency- and temperature-dependent ac susceptibility studies are required for both at 600 and 2000 Oe dc fields for better insight into the complex magnetic dynamics of **3**.

The temperature dependence of ac susceptibility measurements (Fig. 5 for **1** and **2**, Fig. 6 for **4** and Fig. S12, ESI[†] for **3**) shows that only **1**, **2** and **4** display out-of-phase (χ''_{mol}) ac signals below 10 K at the zero dc field, agreed well with the field-swept ac magnetic susceptibility study, indicating the slow relaxation of the magnetisation behaviours of **1**, **2** and **4** at the zero dc field. These signals are wide and do not show clear maxima above 2 K in the available frequency window, indicating that the relaxation mechanism predominantly proceeds through the quantum tunnelling of magnetisation (QTM) in **1**, **2** and **4**, while it is the

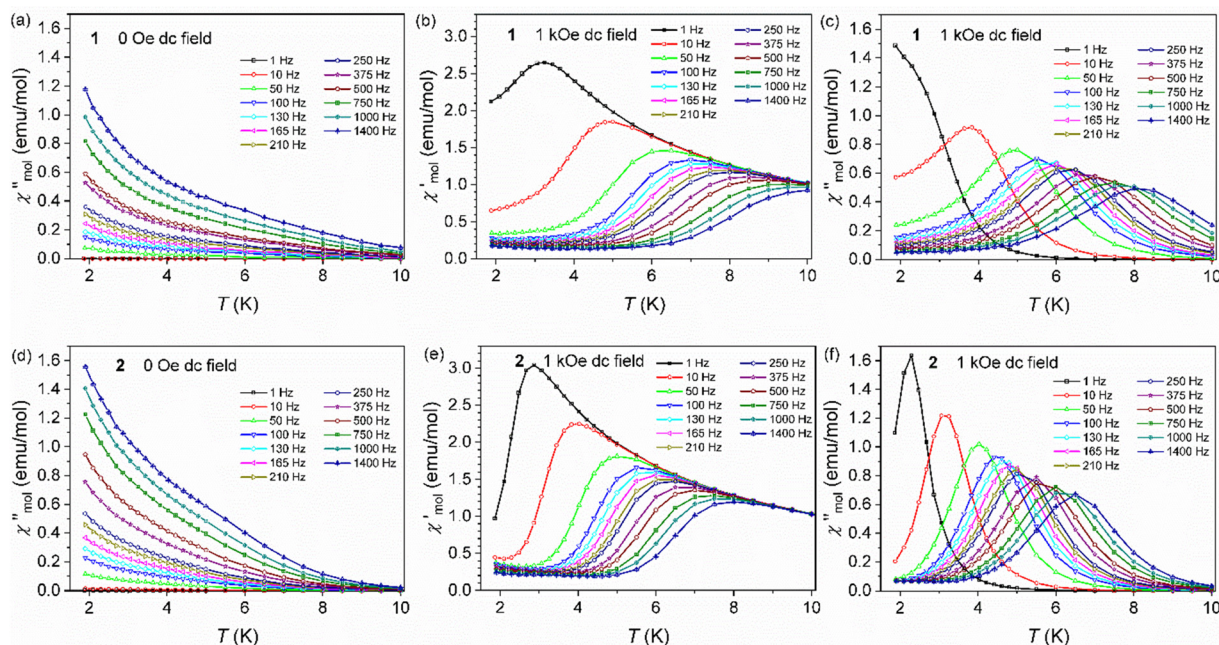


Fig. 5 The variable temperature out-of-phase ac susceptibility data of **1** (a) and **2** (d) in the absence of the dc field and the temperature dependent in-phase and out-of-phase ac susceptibility components in the 1000 Oe dc field of **1** (b and c) and **2** (e and f).

fast enough to display any magnetisation reversal in **3** (Fig. S12, ESI[†]), which could be the reason why these compounds do not display the hysteresis effect at 2 K. An alternative plot of the out-of-phase (χ''_{mol}) ac susceptibility data as a function of the frequency (1–1400 Hz) at different temperatures also shows the monotonous increase of χ''_{mol} with the increasing frequency without any peak up to a 1400 Hz frequency in **1**, **2** and **4**

(Fig. S13, ESI[†]). However, a part of the semi-circular Cole–Cole plot can be constructed and fitted well with a single component generalized Debye model (Fig. S14, ESI[†]).⁴⁷ The extracted distribution coefficient α values are listed in Table S4–S6 (ESI[†]) for **1**, **2** and **4**, respectively, indicating narrow to moderate distributions of the relaxation times in these systems.⁴⁸ Moreover, the values of $\ln(\tau)$ as a function of T follow a good curvature

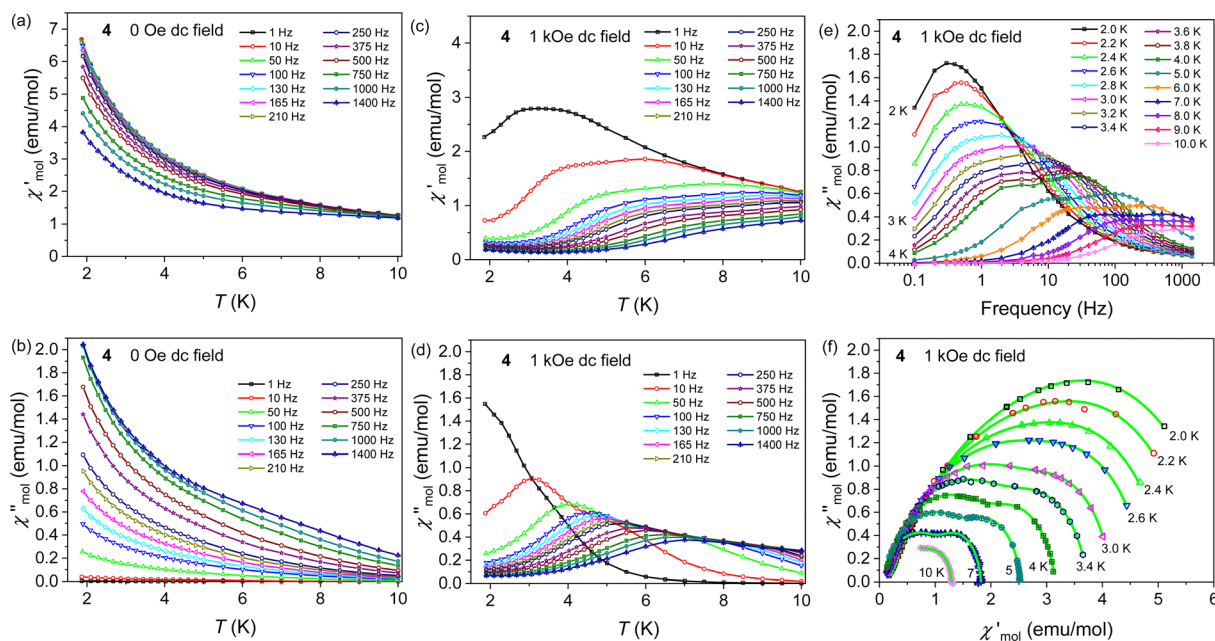


Fig. 6 The variable temperature in-phase and out-of-phase ac susceptibility data of **4** in the absence of the dc field (a and b) and at the 1000 Oe dc field (c and d). The frequency dependent out-of-phase ac susceptibility data of **4** (e) and Cole–Cole plot at the 1000 Oe dc field data set (f). The magnetic data are scaled per one Dy(III) ion.

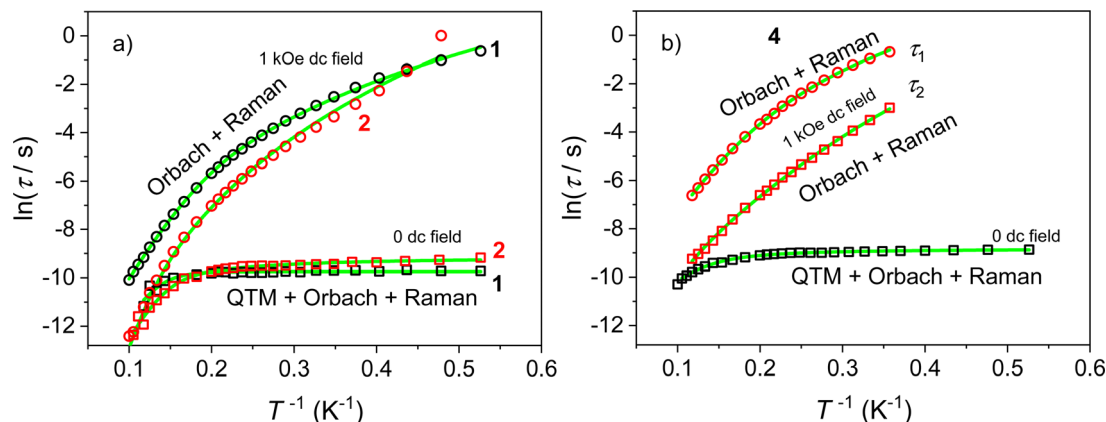


Fig. 7 (a and b) The logarithmic magnetisation relaxation time versus T^{-1} plots for **1** and **2** and **4**, respectively, at indicated dc fields; the solid lines in the plot denote the best simulations based on the multiple relaxation pathways as described in the main text.

pattern (Fig. 7), and thereby a successful attempt was made to analyse these data considering the multiple relaxation mechanism as shown in the following equation:

$$\tau^{-1} = \tau_{\text{QTM}}^{-1} + \tau_0^{-1} \exp(-U_{\text{eff}}/kT) + CT^n \quad (1)$$

where the first term denotes the QTM process, while the second and third ones stand for thermally activated Orbach and two-phonon Raman processes, respectively. To avoid over-parameterization, the n value was fixed to different values until the best correlation coefficient is obtained. The best fitted numerical parameters of **1**, **2** and **4** are presented in Table 2.

The temperature- and frequency-dependent magnetic dynamics of **1**, **2** and **4** were further investigated under the 1000 dc field. The well-shaped peaks with one maximum are observed from 2 to 10 K in both the temperature- and frequency dependent χ''_{mol} plots for **1** and **2** (Fig. 5 and Fig. S15, ESI[†]), indicating that only one relaxation process (LF) is clearly dominant while the other one (HF) is nearly quenched. Moreover, the gradual shifting of both the in-phase and out-of-phase signal maxima to higher frequencies with the increase in temperature indicates the prominent contribution of the thermally activated Orbach process in the slow relaxation mechanism.⁴⁹ From the frequency-dependent ac data at temperatures from 2 to 10 K, a quasi-semicircular shaped Cole–Cole plot (Fig. S16, ESI[†]) can be constructed and fitted with the generalized Debye model for a single-relaxation process to yield a distribution of relaxation times (α values) in the range of 0.02–0.39 (Table S4 and S5, ESI[†]) for **1** and 0.04–0.28 for **2**, indicating a narrow to moderate distribution

of the relaxation times.⁴⁸ In the high temperature region, the distributions are very narrow, suggesting a thermally activated Orbach relaxation mechanism. When the temperature decreases, the distributions are rather broad indicating that other relaxation mechanisms such as Raman, direct and/or QTM processes are also involved.²⁹ The $\ln(\tau)$ vs. T plots (Fig. 7) deviate from the linearity and remain curvature without any indication of the saturation level until the lowest measured temperature 2 K is reached, which indicate the involvement of multi-relaxation pathways and thereby modelled with only Orbach and Raman terms as given in eqn (1), and the best fitting results of **1** and **2** are presented in Table 2.

Unlike **1** and **2**, both temperature- and frequency-dependent ac susceptibility measurements at 1000 Oe for **4** reveal two overlapping out-of-phase (χ''_{mol}) peaks clearly visible and both shift to higher frequencies with the increase in temperature and finally merge and became broad (Fig. 6), suggesting the presence of two thermally activated closely associated relaxation processes.⁵⁰ This behaviour usually observes in multinuclear systems with two distinct Dy(III) ions.⁵¹ In **4**, the asymmetric unit contains two Zn–Dy complex molecules in which Dy(III) ions reside in two different coordination environments, *viz.* a muffin like geometry with C_s symmetry and a spherical capped square antiprism with D_{4d} symmetry as described in the structural section, which might translate into two relaxation processes. The dual relaxation process is also confirmed by the Cole–Cole plots, displaying two overlapping semicircles (Fig. 6), which could be well fitted by the two-set generalized Debye model to

Table 2 Parameters fitted for **1–4** by considering multiple relaxation processes at the indicated magnetic field

Complexes	1		2		3		4	
dc field	0 Oe	1000 Oe	0 Oe	1000 Oe	600 Oe	2000 Oe	0 Oe	1000 Oe τ_1 (τ_2)
τ_0 s ⁻¹	$1.5 \cdot 10^{-6}$	$2.7 \cdot 10^{-7}$	$1.1 \cdot 10^{-8}$	$9.7 \cdot 10^{-11}$	$3.4 \cdot 10^{-7}$	$1.1 \cdot 10^{-8}$	$1.8 \cdot 10^{-6}$	$1.7 \cdot 10^{-5}$ ($1.1 \cdot 10^{-5}$)
U_{eff} K ⁻¹	30.5	55.1	59	107	13	28.5	39.3	43.8 (27.6)
C s ⁻¹ K ⁻ⁿ	0.065	0.060	270	0.012	—	—	77.4	0.013 (0.052)
n	5 (fixed)	5.1	2 (fixed)	7.1	—	—	2 (fixed)	4.8 (5.6)
τ_{QTM}	$6.0 \cdot 10^{-5}$	—	$1.0 \cdot 10^{-4}$	—	—	—	$1.5 \cdot 10^{-4}$	—(—)
A s ⁻¹ K ⁻¹	—	—	—	—	—	3570	—	—
R^2	0.99	0.99	0.98	0.99	0.97	0.98	0.99	0.99 (0.99)

extract two distinct sets of relaxation times (τ_1 and τ_2) and their distribution parameters (α_1 and α_2) and the obtained results are summarized in Table S7 (ESI[†]).⁵² In the temperature range of 2–10 K, α_1 values (0.00–0.10) and α_2 values (0.22–0.39) indicate that both thermally activated relaxation processes have a narrow to moderate distribution of the relaxation time. Two sets of relaxation parameters in the format of $\ln(\tau)$ versus $1/T$ plots were analysed considering Orbach and Raman terms from eqn (1) and the resulted best fit relaxation parameters are listed in Table 2.

The temperature- and frequency-dependent magnetic dynamics of **3** were investigated at the 600 Oe dc field that reveal well-shaped peaks with a maximum below 5 K on the χ''_{mol} curves (Fig. 8 and Fig. S17, ESI[†]) especially for higher frequencies. The maxima shift to higher frequencies upon increasing temperatures demonstrates the thermally activated Orbach mechanism of relaxation. These observations suggest that complex **3** might display the characteristic of the slow magnetic relaxation and consequently the SMM behaviour. From the frequency dependent ac data at various temperatures, a part of the semi-circular Cole–Cole plot was constructed and fitted using the single-set generalized Debye model (Fig. S17, ESI[†]) to extract relaxation times and its distribution factor α varying in the range of 0.13–0.23 (Table S8, ESI[†]), indicating a moderate distribution of relaxation times.⁴⁷ The linear $\ln(\tau)$ vs. T data plot (Fig. S17, ESI[†]) was modelled with only the Orbach term in eqn (1) to yield the best-fit parameters as given in Table 2. Interestingly, when ac measurements were carried out at the 2000 Oe dc field, low frequency (LF) and intermediate frequency (IF) relaxation channels appear in addition to the HF relaxation channel, which is consistent with the field-swept ac data at 2 K for complex **3**. However, this multi-relaxation process is quite different from that observed in **4**, as unlike **4**, complex **3** is consisted with only one type of the Dy(III) ion. However, this type of multiple relaxation process is not unusual for mononuclear Dy(III) systems as there are many examples of SMMs having at least two relaxation pathways, and it was theoretically found that these multiple relaxation pathways can be of intramolecular and/or intermolecular origin.⁵³ Further inspection shows that at low temperatures all three relaxation processes are clearly visible, but with the increase in

temperature, the IF relaxation process is sandwiched by HF and LF relaxation processes, which is clearly seen from the corresponding Cole–Cole plots. The three-set Debye model was applied to fit the data and the resulting distribution parameters and relaxation times are given in Table S9 (ESI[†]). The $\ln(\tau)$ vs. T data set for high-frequency relaxation process can be modelled by considering an additional direct process to the Orbach mechanism that applied for the 600 Oe data set using eqn (2) and the resulting best fit relaxation parameters are given in Table 2.

$$\tau^{-1} = \tau_0^{-1} \exp(-U_{\text{eff}}/kT) + AT \text{ (Orbach + Direct)} \quad (2)$$

Theoretical calculations

To further analyse the magnetic properties of these closely related complexes, the state average complete active space self-consistent field (SA-CASSCF)⁵⁴ calculations followed by SINGLE_ANISO analysis⁵⁵ were performed for molecular structures [ZnDy(L)(NO₃)₃(py)] of **1**, [ZnDy(L)(μ -OAc)(OAc)₂] of **2**, [ZnDy(L)(μ -OAc)(OAc)(NO₃)] of **3**, [ZnDy(L)(μ -piv)(piv)₂] of **4** (further referenced as **4-A**) and [ZnDy(L)(μ -piv)(piv)(OAc)] of **4** (further referenced as **4-B**). The active space was defined by seven f-orbitals of Dy(III) ions containing nine electrons, CAS(9e,7o), which resulted in 21 sextets, 224 quartets, and 490 doublets. The calculated splitting of the ⁶H_{15/2} term for Dy(III) ions in **1–4** spans the energy interval ~600 cm⁻¹ as depicted in Fig. S19 (ESI[†]). The large axial anisotropy of the ground states, $g_z \gg g_x, g_y$, was found in all compounds except for **3** (Table S10–S14, ESI[†]) and the respective g -tensors are shown in Fig. S20 (ESI[†]). The corresponding matrix elements of the transversal magnetic moment among three lowest Kramers doublets (KDs) are shown in Fig. 9 showing possible relaxation pathways in these compounds. It can be deduced that complexes **1**, **2** and **4** have potential to behave as the zero-field SMM, because the corresponding matrix elements of the transversal magnetic moment between ground states with opposite magnetization (0.003 for **1**, 0.005 for **2**, 0.05 for **4-A**, 0.004 for **4-B**) are smaller than 0.1 suggesting the suppression of the quantum tunnelling of the magnetization. This is in good agreement with the experimental observation – the non-zero out-of-phase signal of

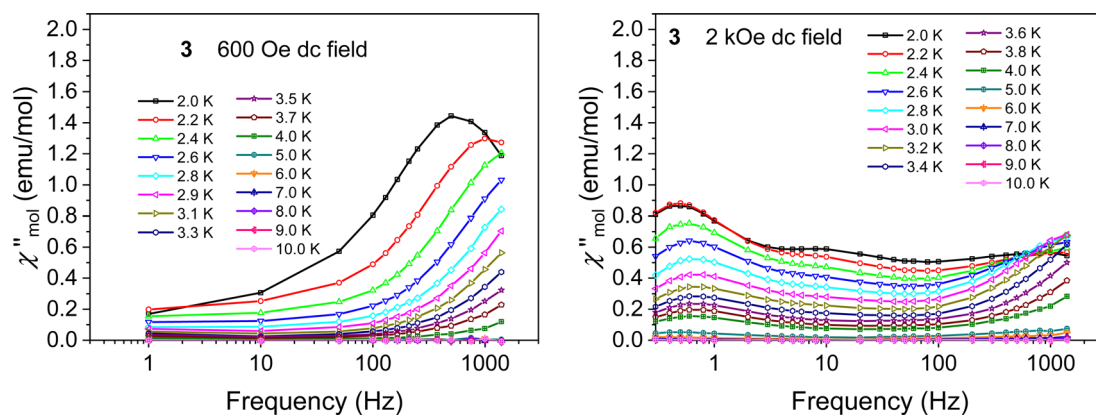


Fig. 8 Frequency dependent out-of-phase ac susceptibility data of **3** at the 600 Oe (left) and 2000 Oe (right) dc fields.

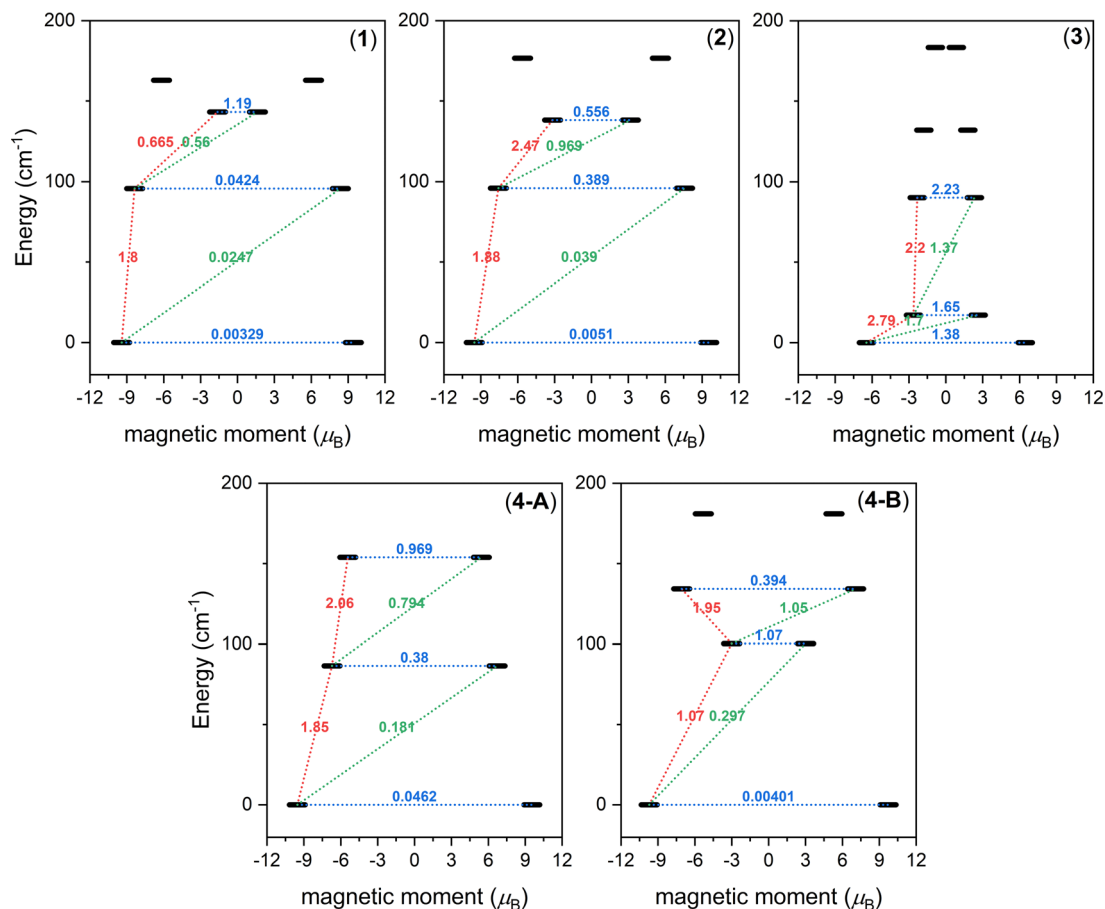


Fig. 9 The plot of SINGLE_ANISO calculations for Dy(III) complexes of **1–4**. The numbers presented for lowest three doublets represent the corresponding matrix element of the transversal magnetic moment (for values larger than 0.1 an efficient relaxation mechanism is expected). The dashed lines refer to (temperature assisted) quantum tunnelling (blue), Orbach/Raman mechanisms (red) and direct/Raman mechanisms (green).

ac susceptibility was found for these compounds. The energies of the first excited Kramers doublets are very similar for **1**, **2** and **4** (96 cm⁻¹ for **1**, 96 cm⁻¹ for **2**, 86 cm⁻¹ for **4-A** and 100 cm⁻¹ for **4-B**) and it is expected that these values are limiting for U_{eff} , because the quantum tunnelling is very likely to apply within these states, except for complex **1**, in which sufficiently large values of the corresponding matrix elements of the transversal magnetic moment are found for the second excited state located at 143 cm⁻¹ (Fig. 9). In the case of complex **3**, the calculated large values for the transversal magnetic moment and the low-lying excited state at 17 cm⁻¹ makes it a poor candidate for the SMM.

Careful inspection of the orientations of the magnetic easy axes of the ground KDs in **1** and **2** reveals the right orientation of the easy axis along the direction of the shortest Dy–O phenolate bonds, suitable for the stability of the oblate electronic cloud of the Dy(III) ions and to enhance the magnetic anisotropy and hence display better SMM behaviours. However, the Dy(III)···Dy(III) intermolecular separation is not large enough to suppress significantly the dipole–dipole interaction and hence to prevent the under barrier relaxation processes such as QTM, and thus the external magnetic field is required to enhance the SMM performance of these complexes. The differences in the SMM properties of **1** and **2** mainly appeared from their

coordination environmental and geometrical differences as it is deca-coordinated in **1** while it is nona-coordinated in **2**. The formation of complex **3** can be considered as if a bidentate acetate ligand in **2** is replaced by a nitrate ion in **3**, but such a small change brings the dramatic influence in the SMM behaviour of these compounds. In both these complexes, the coordination environment, geometry and the extent of deviation from the ideal geometry of the Dy centres as suggested by ChSM values are almost similar, but in **3**, the easy axis is directed to the bridging acetate group with that of the intermediate bond distance, while the shortest Dy–O phenolate bonds are practically directed to the hard plane. Such an arrangement of the anionic donor sites is not suitable for the stabilisation of the oblate electronic distribution in Dy(III) ions, leading to significant transverse magnetic anisotropy in the system, which is further influenced by the relatively strong dipole–dipole interaction of the Dy centres as the Dy···Dy intermolecular separation is the shortest (7.122 Å) in **3** among all these complexes and hence displays the poor SMM performance. The structure of **4** is very similar to complex **2** with only difference that there are two crystallographically distinguishable complex molecules present in **4**. The Dy centre in **4-A** is situated in the relatively higher local symmetry (D_{4d}), while it is placed in

the C_s local symmetry in **4-B**, indicating that the Dy centre in **4-A** could display the better SMM behaviour than that in **4-B**. But in reality, we have not observed much differences in their magnetic behaviours which could be again explained by the orientation of the magnetic easy axis on the Dy centres. Whereas the alignment of the easy axis in **4-B** is very similar to that found in complex **2**, the shortest Dy–O phenolate bond deviates significantly from the easy axis and is closer to the hard plane in **4-A**, which is related to the low axial ligand field and, in turn, displays the mediocre SMM behaviour. To sum up, the magnetic relaxation behaviour is sensitive to subtle differences in the donor sites of the coordinated ligands, which are regulated by the simple co-ligands like acetate, nitrate and pivalate.

The concluding remarks

We have successfully synthesised four new heterometallic ZnDy complexes (**1–4**) using a salen-type classical compartmental ligand (H_2L), derived from a methyl substituted *o*-vanillin in the presence of different co-ligands such as nitrate, acetate and pivalate with the aim to unveil the influence of the co-ligands on the SMM performance of these complexes. The structural characterisation showed that all these complexes possess a nearly identical $[Zn(II)-Dy(III)]$ core bridged by the phenoxo-O atoms of the compartmental Schiff base ligand. The structures of **2–4** are almost identical in that the Dy centres are non-coordinated with an O_9 donor set, while it is deca-coordinated with O_{10} donor atoms in **1**. Magnetic studies revealed that **1**, **2** and **4** can display slow magnetic relaxation at a zero dc field, the performance of which can be further improved at the expense of the reduction of under barrier relaxation processes such as QTM in the presence of an external magnetic field. On the other hand, complex **3** shows a field-induced weaker slow magnetic relaxation behaviour. Moreover, unlike **2** or **4**, complex **3** displays three relaxation processes at higher magnetic fields and especially at low temperatures. *Ab initio* calculations suggest that the better orientations of the magnetic easy axes in **1** and **2** lead to the high axial magnetic anisotropy and hence the high performance of SMM behaviours in these complexes, while the non-ideal alignment of the magnetic easy axis brings weaker magnetic anisotropy and hence the poor SMM character in **3**. An intermediate impression has been observed for complex **4**. Overall, the present report discloses that the magnetic anisotropy on the Dy centre is sensitive to the bridging/chelating co-ligands used, leading to the distinct magnetic dynamics in these systems.

Conflicts of interest

There are no conflicts to declare.

Acknowledgements

A. P. gratefully acknowledges financial support of this work by the Government of West Bengal through the Department of Science & Technology and Biotechnology, Kolkata, India (Sanction No. 331/

ST/P/S&T/15G-8/2018, dated-19.06.2019). Z. J. acknowledges financial support of the Slovenian Research Agency (Grant No. P2-0348). R. H. acknowledges financial support from the institutional sources of the Department of Inorganic Chemistry, Palacký University Olomouc, Czech Republic.

References

- (a) R. Sessoli, D. Gatteschi, A. Caneschi and M. A. Novak, *Nature*, 1993, **365**, 141–143; (b) M. Mannini, F. Pineider, P. Saintavitt, C. Danieli, E. Otero, C. Sciancalepore, A. M. Talarico, M. A. Arrio, A. Cornia, D. Gatteschi and R. Sessoli, *Nat. Mater.*, 2009, **8**, 194–197; (c) S. Thiele, F. Balestro, R. Ballou, S. Klyatskaya, M. Ruben and W. Wernsdorfer, *Science*, 2014, **344**, 1135–1138; (d) M. Shiddiq, D. Komijani, Y. Duan, A. Gaitaariño, E. Coronado and S. Hill, *Nature*, 2016, **531**, 348–351; (e) Y.-J. Ma, J.-X. Hu, S.-D. Han, J. Pan, J.-H. Li and G.-M. Wang, *J. Am. Chem. Soc.*, 2020, **142**, 2682–2689; (f) J. D. Hilgar, M. G. Bernbeck and J. D. Rinehart, *J. Am. Chem. Soc.*, 2019, **141**, 1913–1917.
- (a) P. Zhang, Y. N. Guo and J. Tang, *Coord. Chem. Rev.*, 2013, **257**, 1728–1763; (b) D. N. Woodruff, R. E. P. Winpenny and R. A. Layfield, *Chem. Rev.*, 2013, **113**, 5110–5148; (c) F. Habib and M. Murugesu, *Chem. Soc. Rev.*, 2013, **42**, 3278–3288; (d) S. T. Liddle and J. van Slageren, *Chem. Soc. Rev.*, 2015, **44**, 6655–6669; (e) Z.-P. Ni, J.-L. Liu, M. N. Hoque, W. Liu, J.-Y. Li, Y.-C. Chen and M.-L. Tong, *Coord. Chem. Rev.*, 2017, **335**, 28–43; (f) Z. Zhu, M. Guo, X.-L. Li and J. Tang, *Coord. Chem. Rev.*, 2019, **378**, 350–364.
- (a) K. C. Mondal, A. Sundt, Y. H. Lan, G. E. Kostakis, O. Waldmann, L. Ungur, L. F. Chibotaru, C. E. Anson and A. K. Powell, *Angew. Chem., Int. Ed.*, 2012, **124**, 7668–7672; (b) S. P. Bera, A. Mondal and S. Konar, *Inorg. Chem. Front.*, 2020, **7**, 3352–3363.
- (a) F. S. Guo, B. M. Day, Y. C. Chen, M. L. Tong, A. Mansikkamäki and R. A. Layfield, *Angew. Chem., Int. Ed.*, 2017, **129**, 11603–11607; (b) F.-S. Guo, B. M. Day, Y.-C. Chen, M.-L. Tong, A. Mansikkamäki and R. A. Layfield, *Science*, 2018, **362**, 1400–1403; (c) Z. Zhu, C. Zhao, T. Feng, X. Liu, X. Ying, X.-L. Li, Y.-Q. Zhang and J. Tang, *J. Am. Chem. Soc.*, 2021, **143**(27), 10077–10082.
- (a) C. A. P. Goodwin, F. Ortu, D. Reta, N. F. Chilton and D. P. Mills, *Nature*, 2017, **548**, 439–442; (b) K. R. McClain, C. A. Gould, K. Chakarawet, S. J. Teat, T. J. Groshens, J. R. Long and B. G. Harvey, *Chem. Sci.*, 2018, **9**, 8492–8503.
- (a) Y. Gil, L. Llanos, P. Cancino, P. Fuentealba, A. Vega, E. Spodine and D. Aravena, *J. Phys. Chem. C*, 2020, **124**, 5308–5320; (b) K. L. M. Harriman, J. Murillo, E. A. Sutorina, S. Fortier and M. Murugesu, *Inorg. Chem. Front.*, 2020, **7**, 4805–4812; (c) C. A. Gould, E. Mu, V. Vieru, L. E. Darago, K. Chakarawet, M. I. Gonzalez, S. Demir and J. R. Long, *J. Am. Chem. Soc.*, 2020, **142**, 21197–21209; (d) J. P. Durrant, B. M. Day, J. Tang, A. Mansikkamäki and R. Layfield, *Angew. Chem., Int. Ed.*, 2022, **61**, e202200525; (e) A. Dey, S. Das, S. Kundu, A. Mondal, M. Rouzières, C. Mathonière, R. Clérac, R. S. Narayanan and V. Chandrasekhar, *Inorg. Chem.*, 2017, **56**, 14612–14623.

- 7 (a) J. Li, S. Gómez-Coca, B. S. Dolinar, L. Yang, F. Yu, M. Kong, Y.-Q. Zhang, Y. Song and K. R. Dunbar, *Inorg. Chem.*, 2019, **58**, 2610–2617; (b) S. K. Gupta, S. Dey, T. Rajeshkumar, G. Rajaraman and R. Murugavel, *Chem. – Eur. J.*, 2022, **28**, e202103585; (c) A. B. Canaj, M. K. Singh, C. Wilson, G. Rajaraman and M. Murrie, *Chem. Commun.*, 2018, **54**, 8273–8276; (d) Y. S. Ding, N. F. Chilton, R. E. P. Winpenny and Y. Z. Zheng, *Angew. Chem., Int. Ed.*, 2016, **55**, 16071–16074; (e) J. Liu, Y. C. Chen, J. L. Liu, V. Vieru, L. Ungur, J. H. Jia, L. F. Chibotaru, Y. Lan, W. Wernsdorfer, S. Gao, X. M. Chen and M. L. Tong, *J. Am. Chem. Soc.*, 2016, **138**, 5441–5450; (f) X.-L. Ding, Y.-Q. Zhai, T. Han, W.-P. Chen, Y.-S. Ding and Y.-Z. Zheng, *Chem. – Eur. J.*, 2021, **27**, 2623–2627; (g) F.-X. Shen, K. Pramanik, P. Brandão, Y.-Q. Zhang, N. C. Jana, X.-Y. Wang and A. Panja, *Dalton Trans.*, 2020, **49**, 14169–14179; (h) F. S. Guo, B. M. Day, Y. C. Chen, M. L. Tong, A. Mansikkamaki and R. A. Layfield, *Angew. Chem., Int. Ed.*, 2017, **56**, 11445–11449.
- 8 (a) J. Wang, Q.-W. Li, S.-G. Wu, Y.-C. Chen, R.-C. Wan, G.-Z. Huang, Y. Liu, J.-L. Liu, D. Reta, M. J. Giansiracusa, Z.-X. Wang, N. F. Chilton and M.-L. Tong, *Angew. Chem., Int. Ed.*, 2021, **60**, 5299–5306; (b) M. Kong, X. Feng, J. Wang, Y.-Q. Zhang and Y. Song, *Dalton Trans.*, 2020, **50**, 568–577; (c) K. Pramanik, Y.-C. Sun, P. Brandão, N. C. Jana, X.-Y. Wang and A. Panja, *New J. Chem.*, 2022, **46**, 11722–11733; (d) P. Cen, X. Liu, Y.-Q. Zhang, J. Ferrando-Soria, G. Xie, S. Chen and E. Pardo, *Dalton Trans.*, 2020, **49**, 808–816.
- 9 (a) M. N. Akhtar, M. A. Aldamen, C. D. McMillen, A. Escuer and J. Mayans, *Inorg. Chem.*, 2021, **60**, 9302–9308; (b) A. Dey, P. Bag, P. Kalita and V. Chandrasekhar, *Coord. Chem. Rev.*, 2021, **432**, 213707–213774; (c) Y. Peng and A. K. Powell, *Coord. Chem. Rev.*, 2021, **426**, 213490–213538.
- 10 (a) M. Fondo, J. Corredoira-Vázquez, A. Herrera-Lanzós, A. M. García-Deibe, J. Sanmartín-Matalobos, J. M. Herrera, E. Colacio and C. Nuñez, *Dalton Trans.*, 2017, **46**, 17000–17009; (b) A. Upadhyay, C. Das, S. Vaidya, S. K. Singh, T. Gupta, R. Mondol, S. K. Langley, K. S. Murray, G. Rajaraman and M. Shanmugam, *Chem. – Eur. J.*, 2017, **23**, 4903–4916.
- 11 A. Upadhyay, S. K. Singh, C. Das, R. Mondol, S. K. Langley, K. S. Murray, G. Rajaraman and M. Shanmugam, *Chem. Commun.*, 2014, **50**, 8838–8841.
- 12 (a) C. L. Yin, Z. B. Hu, Q. Q. Long, H. S. Wang, J. Li, Y. Song, Z. C. Zhang, Y. Q. Zhang and Z. Q. Pan, *Dalton Trans.*, 2019, **48**, 512–522; (b) H.-S. Wang, C.-L. Yin, Z.-B. Hu, Y. Chen, Z.-Q. Pan, Y. Song, Y.-Q. Zhang and Z.-C. Zhang, *Dalton Trans.*, 2019, **48**, 10011–10022; (c) J.-Y. Ge, Z. Chen, Y.-R. Qiu, D. Huo, Y.-Q. Zhang, P. Wang and J.-L. Zuo, *Inorg. Chem.*, 2019, **58**, 9387–9396.
- 13 (a) M. Andruh, *Dalton Trans.*, 2015, **44**, 16633–16653; (b) J. Mayans, Q. Saez, M. Font-Bardiabc and A. Escuer, *Dalton Trans.*, 2019, **48**, 641–652; (c) A. Vráblová, M. Tomás, L. R. Falvello, Ľ. Dlhán, J. Titiš, J. Černák and R. Boča, *Dalton Trans.*, 2019, **48**, 13943–13952.
- 14 (a) S. Wang, X. Yang, J. Qian, Q. Li, Z. Chen, L. Zhang, S. Huang, C. Wang and R. A. Jones, *Dalton Trans.*, 2017, **46**, 1748–1752; (b) H. L. C. Feltham and S. Brooker, *Coord. Chem. Rev.*, 2014, **276**, 1–33; (c) A. Dey, J. Acharya and V. Chandrasekhar, *Chem. – Asian J.*, 2019, **14**, 4433–4453; (d) G. Brunet, D. A. Safin, J. Jover, E. Ruiz and M. Murugesu, *J. Mater. Chem. C*, 2017, **5**, 835–841; (e) M. Biswas, E. C. Sañudo and D. Ray, *Inorg. Chem.*, 2021, **60**, 11129–11139.
- 15 A. Panja, Z. Jagličić, R. Herchel, P. Brandão, K. Pramanik and N. C. Jana, *New J. Chem.*, 2022, **46**, 5627–5637.
- 16 A. Panja, Z. Jagličić, R. Herchel, P. Brandão, K. Pramanik and N. C. Jana, *New J. Chem.*, 2022, **46**, 13546–13557.
- 17 G. M. Sheldrick, *SADABS*, University of Göttingen; Germany, 1996.
- 18 G. M. Sheldrick, *Acta Crystallogr., Sect. A: Found. Crystallogr.*, 2008, **64**, 112.
- 19 (a) F. Neese, *Wiley Interdiscip. Rev.: Comput. Mol. Sci.*, 2012, **2**, 73–78; (b) F. Neese, *Wiley Interdiscip. Rev.: Comput. Mol. Sci.*, 2018, **8**, e1327; (c) F. Neese, F. Wennmohs, U. Becker and C. Riplinger, *J. Chem. Phys.*, 2020, **152**, 224108–224125; (d) F. Neese, Software update: The ORCA program system—Version 5.0, *Wiley Interdiscip. Rev.: Comput. Mol. Sci.*, 2022, e1606.
- 20 (a) M. Douglas and N. M. Kroll, *Ann. Phys.*, 1974, **82**, 89–155; (b) B. A. Hess, *Phys. Rev. A: At., Mol., Opt. Phys.*, 1986, **33**, 3742–3748.
- 21 L. Visscher and K. G. Dyall, *At. Data Nucl. Data Tables*, 1997, **67**, 207–224.
- 22 (a) F. Weigend and R. Ahlrichs, *Phys. Chem. Chem. Phys.*, 2005, **7**, 3297–3305; (b) D. Aravena, F. Neese and D. A. Pantazis, *J. Chem. Theory Comput.*, 2016, **12**, 1148–1156.
- 23 D. A. Pantazis and F. Neese, *J. Chem. Theory Comput.*, 2009, **5**, 2229–2238.
- 24 G. L. Stoychev, A. A. Auer and F. Neese, *J. Chem. Theory Comput.*, 2017, **13**, 554–562.
- 25 (a) F. Neese, F. Wennmohs, A. Hansen and U. Becker, *Chem. Phys.*, 2009, **356**, 98–109; (b) R. Izsák and F. Neese, *J. Chem. Phys.*, 2011, **135**, 144105–144115.
- 26 C. Adamo and V. Barone, *J. Chem. Phys.*, 1999, **110**, 6158–6170.
- 27 E. Caldeweyher, S. Ehlert, A. Hansen, H. Neugebauer, S. Spicher, C. Bannwarth and S. Grimme, *J. Chem. Phys.*, 2019, **150**, 154122–154140.
- 28 K. Momma and F. Izumi, *J. Appl. Crystallogr.*, 2011, **44**, 1272–1276.
- 29 Z.-Y. Zhao, H.-H. Xu, P. Chen, Y.-X. Li, Y. Sui and W.-B. Sun, *J. Mater. Chem. C*, 2020, **8**, 4843–4850.
- 30 A.-L. Boulkedid, A. Beghidja, C. Beghidja, Y. Guari, J. Larionova and J. Long, *Dalton Trans.*, 2019, **48**, 11637–11641.
- 31 B. El Rez, J. Liu, V. Béreau, C. Duhayon, Y. Horino, T. Suzuki, L. Coolen and J.-P. Sutter, *Inorg. Chem. Front.*, 2020, **7**, 4527–4534.
- 32 V. Béreau, S. Dhers, J.-P. Costes, C. Duhayon and J.-P. Sutter, *Eur. J. Inorg. Chem.*, 2018, 66–73.
- 33 J. P. Costes, S. Titos-Padilla, I. Oyarzabal, T. Gupta, C. Duhayon, G. Rajaraman and E. Colacio, *Inorg. Chem.*, 2016, **55**, 4428–4440.
- 34 A. Watanabe, A. Yamashita, M. Nakano, T. Yamamura and T. Kajiwara, *Chem. – Eur. J.*, 2011, **17**, 7428–7432.

- 35 P. Zhang, L. Zhang, S.-Y. Lin and J. Tang, *Inorg. Chem.*, 2013, **52**, 6595–6602.
- 36 J. Long, R. Vallat, R. A. S. Ferreira, L. D. Carlos, F. A. Almeida Paz, Y. Guaría and J. Larionova, *Chem. Commun.*, 2012, **48**, 9974–9976.
- 37 H.-R. Wen, J.-J. Hu, K. Yang, J.-L. Zhang, S.-J. Liu, J.-S. Liao and C.-M. Liu, *Inorg. Chem.*, 2020, **59**, 2811–2824.
- 38 A.-L. Boulkedid, J. Long, C. Beghidja, Y. Guari, A. Beghidja and J. Larionova, *Dalton Trans.*, 2018, **47**, 1402–1406.
- 39 J. P. Costes, S. Titos-Padilla, I. Oyarzabal, T. Gupta, C. Duhayon, G. Rajaraman and E. Colacio, *Chem. – Eur. J.*, 2015, **21**, 15785–15796.
- 40 W.-B. Sun, P.-F. Yan, S.-D. Jiang, B.-W. Wang, Y.-Q. Zhang, H.-F. Li, P. Chen, Z.-M. Wang and S. Gao, *Chem. Sci.*, 2016, **7**, 684–691.
- 41 P. L. Then, C. Takehara, Y. Kataoka, M. Nakano, T. Yamamura and T. Kajiwara, *Dalton Trans.*, 2015, **44**, 18038–18048.
- 42 M. Maeda, S. Hino, K. Yamashita, Y. Kataoka, M. Nakano, T. Yamamura and T. Kajiwara, *Dalton Trans.*, 2012, **41**, 13640–13648.
- 43 P.-Y. Shan, H.-F. Li, P. Chen, Y.-M. Tian, W.-B. Sun and P.-F. Yan, *Z. Anorg. Allg. Chem.*, 2015, **641**, 1119–1124.
- 44 M. Llunell, D. Casanova, J. Cirera, P. Alemany and S. Alvarez, *SHAPE, version 2.1*, Universitat de Barcelona, Barcelona, Spain, 2013.
- 45 (a) S. Biswas, S. Das, T. Gupta, S. K. Singh, M. Pissas, G. Rajaraman and V. Chandrasekhar, *Chem. – Eur. J.*, 2016, **22**, 18532–18550; (b) J. Lu, V. Montigaud, O. Cador, J. Wu, L. Zhao, X.-L. Li, M. Guo, B. Le Guennic and J. Tang, *Inorg. Chem.*, 2019, **58**, 11903–11911; (c) G. M. Risica, V. Vieru, B. O. Wilkins, T. P. Latendresse, J. H. Reibenspies, N. S. Bhuvanesh, G. P. Wylie, L. F. Chibotaru and M. Nippe, *Angew. Chem., Int. Ed.*, 2020, **59**, 13335–13340.
- 46 (a) K. R. Vignesh, D. I. Alexandropoulos, H. Xie and K. R. Dunbar, *Dalton Trans.*, 2020, **49**, 4694–4698; (b) F.-X. Shen, H.-Q. Li, H. Miao, D. Shao, X.-Q. Wei, L. Shi, Y.-Q. Zhang and X.-Y. Wang, *Inorg. Chem.*, 2018, **57**, 15526–15536; (c) H.-Q. Li, Y.-C. Sun, L. Shi, F.-L. Chen, F.-X. Shen, Y. Zhao and X.-Y. Wang, *Inorg. Chem.*, 2022, **61**, 2272–2283.
- 47 (a) Y.-N. Guo, G.-F. Xu, Y. Guo and J. Tang, *Dalton Trans.*, 2011, **40**, 9953–9963; (b) D. Reta and N. F. Chilton, *Phys. Chem. Chem. Phys.*, 2019, **21**, 23567–23575.
- 48 (a) Y.-X. Qu, Z.-Y. Ruan, G.-Z. Huang, Y.-C. Chen, Y. Liu, J.-H. Jia, J.-L. Liu and M.-L. Tong, *Inorg. Chem. Front.*, 2021, **8**, 4657–4665; (b) Y. Fang, R. Sun, A.-H. Sun, H.-L. Sun and S. Gao, *Dalton Trans.*, 2021, **50**, 1246–1252; (c) X. Cai, Z. Cheng, Y. Wu, R. Jing, S.-Q. Tian, L. Chen, Z.-Y. Li, Y.-Q. Zhang, H.-H. Cui and A. Yuan, *Inorg. Chem.*, 2022, **61**, 3664–3673.
- 49 F.-S. Guo, M. He, G.-Z. Huang, S. R. Giblin, D. Billington, F. W. Heinemann, M.-L. Tong, A. Mansikkamäki and R. A. Layfield, *Inorg. Chem.*, 2022, **61**, 6017–6025.
- 50 J. Wu, S. Demeshko, S. Dechert and F. Meyer, *Dalton Trans.*, 2021, **50**, 17573–17582.
- 51 (a) I. F. Díaz-Ortega, J. M. Herrera, D. Aravena, E. Ruiz, T. Gupta, G. Rajaraman, H. Nojiri and E. Colacio, *Inorg. Chem.*, 2018, **57**, 6362–6375; (b) L. Zhang, J. Jung, P. Zhang, M. Guo, L. Zhao, J. Tang and B. Le Guennic, *Chem. – Eur. J.*, 2016, **22**, 1392–1398; (c) D. Pinkowicz, M. Ren, L. M. Zheng, S. Sato, M. Hasegawa, M. Morimoto, M. Irie, B. K. Breedlove, G. Cosquer, K. Katoh and M. Yamashita, *Chem. – Eur. J.*, 2014, **20**, 12502–12513; (d) J. Lu, Y.-Q. Zhang, X.-L. Li, M. Guo, J. Wu, L. Zhao and J. Tang, *Inorg. Chem.*, 2019, **58**, 5715–5724.
- 52 R. Boča, M. Stolarová, L. R. Falvello, M. Tomás, J. Titiš and J. Černák, *Dalton Trans.*, 2017, **46**, 5344–5351.
- 53 (a) L. T. A. Ho and L. F. Chibotaru, *Phys. Rev. B*, 2016, **94**, 104422–104427; (b) L. T. A. Ho and L. F. Chibotaru, *Phys. Rev. B*, 2018, **98**, 174418–174429; (c) V. S. Parmar, G. K. Gransbury, G. F. S. Whitehead, D. P. Mills and R. E. P. Winpenny, *Chem. Commun.*, 2021, **57**, 9208–9211; (d) P. E. Kazin, M. A. Zykin, L. A. Trusov, A. V. Vasiliev, R. K. Kremer, R. E. Dinnebier and M. Jansen, *Dalton Trans.*, 2020, **49**, 2014–2023.
- 54 P.-Å. Malmqvist and B. O. Roos, *Chem. Phys. Lett.*, 1989, **155**, 189–194.
- 55 L. F. Chibotaru and L. Ungur, *J. Chem. Phys.*, 2012, **137**, 064112–064133.